



Ru doping effect on the structural, electronic, transport, optical and dye degradation properties of layered Li_2MnO_3

Brajendra Singh¹ · Priyanka Singh¹ Received: 30 August 2019 / Accepted: 13 February 2020 / Published online: 28 February 2020
© Springer Nature Switzerland AG 2020

Abstract

Ru doped Li_2MnO_3 compositions show the presence of redox couples $\text{Mn}^{3+}\text{--Mn}^{4+}$ and $\text{Ru}^{4+}\text{--Ru}^{5+}$. Due to the presence of these redox couples in $\text{Li}_2\text{Mn}_{1-x}\text{Ru}_x\text{O}_3$ ($x=0.05, 0.1$), Ru doped compositions show (i) change in structure (ii) large decrease in impedance ($\sim 10^7$ to $\sim 10^5$ Ohm) (iii) degrade methyl orange and methylene blue solution (pH-6) in quick time in presence of tungsten (W) bulb and sun light. Synchrotron X-ray powder diffraction studies show the change in lattice parameters with Ru doping at Mn site in $\text{Li}_2\text{Mn}_{1-x}\text{Ru}_x\text{O}_3$ ($x=0.05, 0.1$). Raman and Infrared spectroscopic studies show the shift in Mn–O stretching mode of Li_2MnO_3 towards lower wave number with Ru doping. Soft X-ray absorption spectroscopic studies show the presence of mixed valences of Mn^{3+} , Mn^{4+} , Ru^{4+} and Ru^{5+} in $\text{Li}_2\text{Mn}_{1-x}\text{Ru}_x\text{O}_3$ ($x=0.05, 0.1$) using $L_{2,3}$ and M_4 edge. UV–Vis diffuse reflectance spectroscopic studies show the optical band gap in visible light range in Ru doped $\text{Li}_2\text{Mn}_{1-x}\text{Ru}_x\text{O}_3$ ($x=0.05, 0.1$) compositions. The presence of 5 mg of $\text{Li}_2\text{Mn}_{0.9}\text{Ru}_{0.1}\text{O}_3$ degrades 5 ml of methyl orange solution (10 mg/L) of pH 6 in 5 min and methylene blue solution (10 mg/L) of pH 6 in 3 min of exposure in W bulb light.

Keywords Synchrotron X-ray · XAS · Raman · Dye degradation · Optical absorption

1 Introduction

Manganese (Mn) containing oxides crystallize in layered, perovskite, spinel, and various other structures, where valence state of Mn make these oxides vulnerable for various technological applications [1–7]. Colossal magnetoresistance, room temperature magnetism, metal to insulator transition, catalytic and Li intercalation are some of the properties which are utilized in devices [1, 2, 5, 6]. Mixed valence states of Mn play a major role in altering the properties of the materials as per the technological application need [2, 6, 7]. In perovskite oxides, ratio of Mn mixed valence $\text{Mn}^{3+}/\text{Mn}^{4+}$ decides the structural, magnetic and transport properties. Mn^{3+} containing oxides show insulating and antiferromagnetic behaviour while Mn^{4+} containing oxides also show insulating and antiferromagnetic

properties [2, 6]. When Mn^{3+} remains present 67% and Mn^{4+} 33% then perovskite oxides show metallic and ferromagnetic behaviour. Presence of 50% Mn^{3+} and 50% Mn^{4+} valence states makes spinel oxides susceptible for charging and discharging in Li ion battery [1, 4, 7].

Hierarchical microstructure of Mn_3O_4 has been tried for degradation of methylene blue [8]. MnO_2 , which has +4 valence state of Mn, has been considered as a photocatalyst and known for its cost effectiveness, adsorption/oxidizing abilities, large specific surface area and nontoxic nature [9]. It has been observed that some of the good photocatalysts involve metal cations Fe^{+2} in photo-fenton process for degradation of MB, where redox interaction between Fe^{+2} and Fe^{+3} play an important role to produce hydroxyl ions [10]. Ru is a 4 d transition metal and placed in same group with iron in periodic table. Ru–Mn interaction

✉ Brajendra Singh, brajendr@gmail.com; brajendr@allduniv.ac.in; Priyanka Singh, priyankauoa@gmail.com | ¹Materials Chemistry Lab, Centre of Material Sciences, University of Allahabad, Allahabad 211002, India.



induces mixed valence $\text{Ru}^{+4}/\text{Ru}^{+5}$ with $\text{Mn}^{+3}/\text{Mn}^{+4}$ in perovskite oxides and spinel structures [11–14]. When Ru^{+4} (0.62 Å) is interact with Mn^{+4} (0.53 Å), it undergo redox reaction which leads to Mn^{+3} (0.645 Å) and Ru^{+5} (0.565 Å) valence states as redox potential of $\text{Ru}^{+4}/\text{Ru}^{+5}$ (1.07 eV) is comparable with that of $\text{Mn}^{+3}/\text{Mn}^{+4}$ (1.02 eV) [15]. $\text{Ru}^{+4}/\text{Ru}^{+5}$ redox couple operates at 4.3 V vs Li in the spinel LiMn_2O_4 and increases the cycling capacity of Li ion battery [12]. Ru doping brings cycling stability due to the presence of $\text{Ru}^{+4}/\text{Ru}^{+5}$ redox couple in $\text{Li}_2\text{Mn}(\text{Ru})\text{O}_3$ rock salt type layered structure [16–19]. Presence of mixed valence $\text{Ru}^{+4}/\text{Ru}^{+5}$ with $\text{Mn}^{+3}/\text{Mn}^{+4}$ brings long range of magnetic ordering in $\text{La}_{0.7}\text{Ca}_{0.3}\text{Mn}_{1-x}\text{Ru}_x\text{O}_3$ thin films [14]. Ru^{+4} containing thin film of $\text{La}_{0.7}\text{Ca}_{0.3}\text{Mn}_{0.7}\text{Ru}_{0.3}\text{O}_3$ shows colossal magnetoimpedance effects at room temperature [20]. Ru exists in its single valence state Ru^{+4} in $\text{LaMn}_{1-x}\text{Ru}_x\text{O}_3$ ($x = 0.1, 0.2, 0.3, 0.4$) compositions and it shows band gap in the range of ~ 1.27 eV to 1.36 eV [21]. $\text{LaMn}_{1-x}\text{Ru}_x\text{O}_3$ compounds degrade MO solution (pH 2.5) and generate photocatalytic oxygen by water in W bulb light [21]. In this study, we have documented the doping effect of Ru^{+4} at Mn^{+4} site in Li_2MnO_3 on the structure, Mn and Ru valence states, and dye degradation properties using methyl orange (MO) and methylene blue (MB) at nominal pH 6.

2 Experimental

Polycrystalline $\text{Li}_2\text{Mn}_{1-x}\text{Ru}_x\text{O}_3$ ($x = 0.0, 0.05, 0.1$) samples were prepared using high temperature solid state reaction route. In the preparation process, we have weighed the stoichiometric amount of high purity $\text{LiOH}\cdot\text{H}_2\text{O}$, MnO_2 and RuO_2 . They were thoroughly mixed in an agate mortar and heated at 950 °C for 12 h in an ambient atmosphere in muffle furnace. $\text{Sr}_4\text{Ru}_2\text{O}_9$ sample was prepared by taking stoichiometric amount of high purity SrCO_3 and RuO_2 oxides. The precursors were thoroughly mixed in an agate mortar and calcined at 850 °C for 36 h in oxygen atmosphere, and subsequently sintered under oxygen atmosphere at 950 °C for 36 h in tubular furnace. LiMn_2O_4 sample was prepared by taking stoichiometric amount of high purity $\text{LiOH}\cdot\text{H}_2\text{O}$ and MnO_2 . The precursors were thoroughly mixed in an agate mortar and heated at 800 °C for 24 h. $\text{LaMn}_{0.8}\text{Ru}_{0.2}\text{O}_3$ sample was prepared by taking stoichiometric amount of high purity La_2O_3 , MnO_2 and RuO_2 oxides. The precursors were thoroughly mixed in an agate mortar and calcined at 900 °C for 24 h and subsequently sintered at 1050 °C for 24 h in ambient atmosphere. Heating rate was maintained 5 °C/min during heating and cooling. The X-ray powder diffraction patterns (step size 0.015, scan speed 1 s/step) using synchrotron radiation ($\lambda = 1.09$ Å) were recorded at room

temperature at Indian beamline BL-18B, Photon Factory (PF), KEK, Tsukuba, Japan. The incoming X-ray beam from the bending magnet of the PF storage ring was collimated with a set of beam-defining slits having vertical opening of 0.2 mm and 2 mm in the horizontal direction. The sample was mounted onto an 8-circle goniometer (Huber, Germany) at the focal point of the focusing mirror of the beamline. A slit of 1.5 mm (horizontal) by 0.25 mm (vertical) was mounted just before the detector to increase the signal-to-background ratio. Raman spectra of these powder samples were recorded using Renishaw micro-Raman spectrometer (model RM-2000) and focused Ar^+ laser beam of 514-nm using Leica microscope. The incident laser power was attenuated to 2 mW, and data acquisition time was set to 50 s for all the samples was used to record the data. The Raman spectra were recorded using Peltier air-cooled CCD detector in the range of 100–3200 cm^{-1} . Fourier transform infrared (FTIR) spectra (absorbance vs. wavenumber) of the samples were recorded using a FTIR Perkin Elmer spectrometer, using the KBr pellet technique from 400 to 4000 cm^{-1} at room temperature. Each IR scan recorded after averaging of 25 scans. X-ray absorption spectroscopy (XAS) measurements for Mn $L_{2,3}$, and Ru $M_{4,5}$ were performed at the Soft X-ray absorption spectroscopy (SXAS) beamline (BL-01) of the INDUS 2 synchrotron source source (2.5 GeV, 300 mA) at Raja Ramanna Centre for Advanced Technology (RRCAT), Indore, India. This beamline is operating in the energy range 100–1200 eV. Sample pellets were mounted in an ultrahigh vacuum (UHV) chamber with a base pressure of 10^{-10} Torr. SXAS data were collected in total electron yield (TEY) mode at room temperature under ultra-high vacuum conditions. Impedance and capacitance measurements were recorded using novacontrol make Impedance analyzer (Alpha-A high performance frequency analyzer) in the frequency range from 1 Hz to 40 MHz in ambient atmosphere at room temperature. We had used 10.4 mm diameter and 1.2 mm thick pellets polished both side with silver paste for these measurements. The wire length was ~ 2 feet between the impedance analyzer and sample. The reflectance of the $\text{Li}_2\text{Mn}_{1-x}\text{Ru}_x\text{O}_3$ ($x = 0.0, 0.05, 0.1$) solid samples were recorded using UV–visible diffuse reflectance spectroscopy (DRS) in a Shimadzu UV-2450 spectrophotometer over a wavelength range of 200–800 nm. BaSO_4 was used as an internal reflectance standard. The absorbance of the Methyl Orange (MO) and Methylene Blue (MB) solution was measured in wavelength range of 200–800 nm to find out the degradation. To find out the band gap of these samples, the diffuse reflectance data were converted to the Kubelka–Munk function by equation [22]:

$$F(R) = (1 - R)^2 / 2R$$

where R is reflectance, $F(R)$ is proportional to extinction coefficient α .

Band gaps were determined by Tauc plots using equation [23]:

$$[\alpha h\nu]^{1/n} = A [h\nu - E_g]$$

where ν is frequency, A is absorption constant, h is Planck constant and E_g is band gap. Here, n denotes the nature of band gap. For indirect band gap $n=2$ and direct band gap $n=1/2$ is used.

To understand the dye degradation ability of $\text{Li}_2\text{Mn}_{1-x}\text{Ru}_x\text{O}_3$ ($x = 0.0$ and 0.1), we have selected methyl orange (MO) and methylene blue (MB) dyes for degradation. MnO_2 has been used as reference for MO and MB degradation. The photocatalytic degradation of aqueous methyl orange and methylene blue dyes by $\text{Li}_2\text{Mn}_{1-x}\text{Ru}_x\text{O}_3$, and MnO_2 , was carried out in a borosil make glass sample vials. Sample vial further placed in ultrasonicator and exposed in visible light of 200 Watt incandescent tungsten (W) bulb (300 to 900 nm) under constant flow of water (to maintain the constant temperature). MO and MB stock solutions of 10 mg/L concentration were prepared in ultra pure water. Hydrochloric acid was used to maintain pH of dye solutions. For dye degradation experiment, we have used 5 mg of catalyst in 5 ml dye solutions of 10 mg/L concentration for all the compositions. Before mixing catalysts in dye solutions, the pH of dye solutions was maintained 6. Ultrasonicator was used for proper mixing of catalyst and dye solution during exposing the mixture in visible light. The distance between 200 W incandescent tungsten(W) bulb and sample vial was maintained 15 cm. Visible part of sample vials (4 cm length and 1.6 cm diameter) was effectively exposed to 70.77 mW/cm^2 power of radiation. The samples were filtered using whatmann filter paper after exposing in W bulb light and absorbance of dye solutions were recorded in a Shimadzo make UV-Visible spectrometer over a wavelength range of 200–800 nm. The concentration of MB were calculated as $C_t = C_0(A_t/A_0)$,

where C_0 - initial MB concentration, A_0 —initial absorbance (at $\lambda = 662 \text{ nm}$), C_t —MB concentration at time t , and A_t —absorbance (at maxima of peak on t minute), respectively. The degradation rate % was calculated by $[(A_0 - A_t)/A_0] \times 100$.

3 Results and discussion

Li_2MnO_3 crystallizes in monoclinic unit cell and space group C2/m (Fig. 1). It is a layered structure, where a layer of Li ions, and a mixed layer of Li and 2Mn ions are alternating between closed packed oxygen layers. In a crystal, Li ions occupy three positions (2b, 2c and 4 h), oxygen ions occupy two positions (4i and 8j) and Mn atom occupies one position (4g) [24, 25]. In MnO_6 octahedra, two types of Mn–O bonds of 1.90 Å and 1.91 Å exists [24, 25].

Figure 2 shows the synchrotron X-ray powder diffraction patterns of $\text{Li}_2\text{Mn}_{1-x}\text{Ru}_x\text{O}_3$ [$x = 0.0, 0.05, 0.1$] compositions from 10 degree to 70 degree. We have found stoichiometric single phase for $\text{Li}_2\text{Mn}_{1-x}\text{Ru}_x\text{O}_3$ [$x = 0.0, 0.05, 0.1$] compositions and diffraction patterns matches with the reference code ICSD-202639 and JCPDS-01-084-1634 patterns. All the peaks are matching with the reported results in literature. Parent and Ru doped diffraction patterns show the characteristic peaks (020), (110), (021) and (110) which confirms the crystallization of these compositions in C2/m. Figure 3 shows the close look of the peaks of normalized intensity for all the compositions. It has been observed that the peaks (001), (020), (110), (130) shifts at lower theta with the increase in Ru concentration. Shifting of peaks shows the expansion of unit cell with Ru substitution due to the higher ionic size of Ru^{+4} (0.76 Å) than the ionic size of Mn^{+4} (0.67 Å). Peaks (202) and (131) merge together with Ru substitution at Mn site. Peak ($\bar{3}31$) shifted towards lower theta value for Ru = 0.05 composition but for Ru-0.1 composition ($\bar{3}31$) peak split into ($\bar{3}31$) and (060). Crystallite size for all the composition has been calculated using Debye Sherrer formula (Crystallite

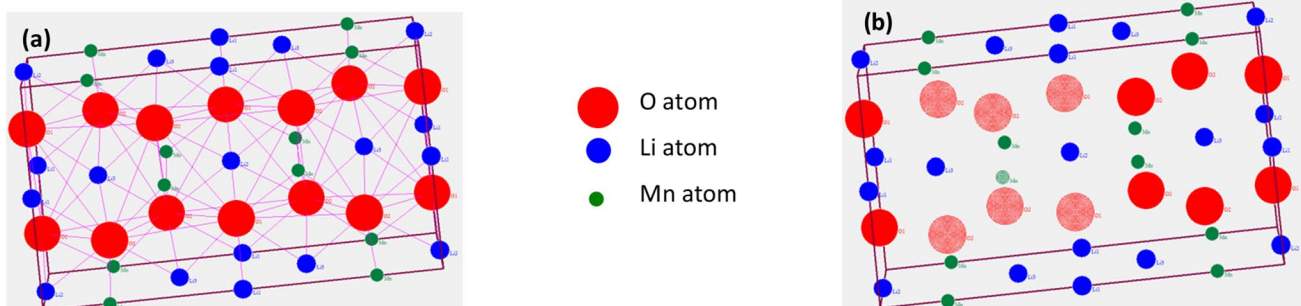


Fig. 1 **a** Crystal structure of monoclinic Li_2MnO_3 . **b** Shaded atoms (six O and one Mn atoms) show the configuration of MnO_6 octahedra in Li_2MnO_3

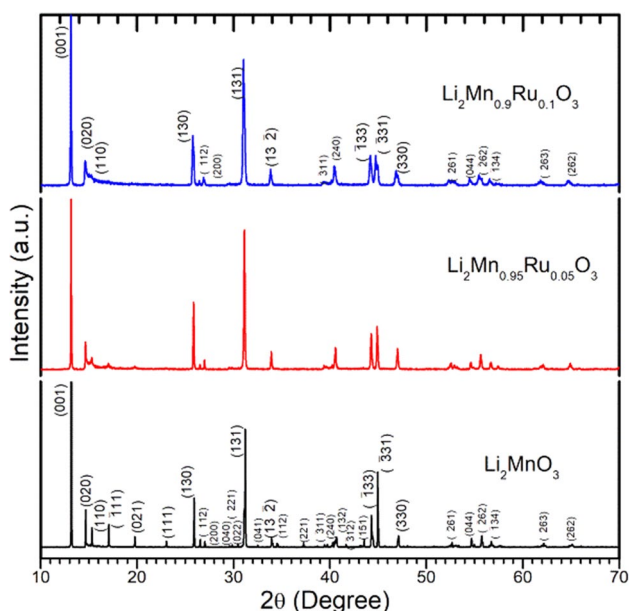


Fig. 2 Synchrotron X-ray powder diffraction patterns of $\text{Li}_2\text{Mn}_{1-x}\text{Ru}_x\text{O}_3$ ($x=0.0, 0.05, 0.1$). Ru doped compositions show the single phase as Li_2MnO_3 . Peaks are indexed for Li_2MnO_3

size (\AA) = $0.9\lambda/d \cos\theta$). Ru doping decreases crystallite size of materials. Table 1 summarizes the results of the analysis of synchrotron X-ray powder diffraction patterns. These results show that Ru has been successfully doped at Mn site in $\text{Li}_2\text{Mn}_{1-x}\text{Ru}_x\text{O}_3$ [$x=0.05, 0.1$]. To explore the shifting of peaks at lower theta value and lowering of crystallite size at micro level by Ru doping at Mn site, we have recorded the Raman spectra of these compositions [12, 26].

Figure 4 shows the Raman peaks for powder samples of $\text{Li}_2\text{Mn}_{1-x}\text{Ru}_x\text{O}_3$ [$x=0.0, 0.05, 0.1$] compositions. Theoretical calculations predict the 15 Raman active optical modes, in which 7 modes are A_g and 8 modes are B_g [27]. In monoclinic space group $C2/m$, A_g modes are generated from the symmetric vibrations of cations along b-axis. B_g modes are generated from the symmetric vibrations of cations along a and c-axis. The vibrations of octahedrally coordinated Mn atom at 4g position results 1 A_g and 2 B_g modes, while 1 A_g and 2 B_g modes are due to Li atom at 4h site. O atom at 4i position generates 2 A_g and 1 B_g modes, and remaining 3 A_g and 3 B_g modes can be assigned to vibrations of O atom at 8j site [28, 29]. We have clearly observed 14 active Raman modes in our synthesized $\text{Li}_2\text{Mn}_{1-x}\text{Ru}_x\text{O}_3$ samples while other groups have reported only 8 Raman peaks in monoclinic Li_2MnO_3 samples [28, 29]. The observed Raman Peaks positions are summarized in Table 2 for $\text{Li}_2\text{Mn}_{1-x}\text{Ru}_x\text{O}_3$ [$x=0.0, 0.05, 0.1$] compositions. Ru substitution at Mn

site shifts A_g peak at $\sim 615 \text{ cm}^{-1}$ of Li_2MnO_3 to lower value $\sim 610.8 \text{ cm}^{-1}$ for $x=0.05$ composition. This observation is similar to the Ru doped LiMn_2O_4 samples where we had observed the peak shifting towards lower wave numbers [12]. Ru as a 4d transition metal having extended orbitals and higher spin orbit coupling constant 800 cm^{-1} in comparison with 100 cm^{-1} of Mn. It makes Ru–O bond stronger than Mn–O bond which reflect in shifting of A_g vibrational peak towards lower wave numbers.

For Ru = 0.1 composition, we have observed that Raman peaks splitted into multiple peaks for stretching modes of Mn–O vibrations, it shows that the multiple cations vibration contributing to stretching modes. Figure 5 shows the Infra red (IR) peaks for powder samples of $\text{Li}_2\text{Mn}_{1-x}\text{Ru}_x\text{O}_3$ [$x=0.0, 0.1$] compositions. Theoretical calculations predict the 7 A_u and 11 B_u IR active optical modes [27]. We have found 7 peaks for Li_2MnO_3 which are similar with the reported experimental studies in literature [30]. In $\text{Li}_2\text{Mn}_{0.9}\text{Ru}_{0.1}\text{O}_3$, some Raman peaks merge and total 5 peaks have been observed. All the peaks have been shifted towards lower wavenumber with the doping of Ru at Mn site. Presence of multiple peaks and shift of other vibrational peaks in Raman and IR spectra motivated us to find the valence states of transition metals Mn and Ru in $\text{Li}_2\text{Mn}_{1-x}\text{Ru}_x\text{O}_3$ [$x=0.05, 0.1$] compositions.

In Figure 6a, we show Mn- $L_{2,3}$ absorption edge spectra of $\text{Li}_2\text{Mn}_{1-x}\text{Ru}_x\text{O}_3$ [$x=0.0, 0.05, 0.1$] and $\text{Li}_2\text{Mn}_2\text{O}_4$ systems together with that of Mn_2O_3 , MnO_2 (where Mn exist in +3 and +4 valence states) for comparison. The L_2 edge and L_3 edge correspond to the $2p_{1/2} - 3d$ (t_{2g} and e_g orbitals) and $2p_{3/2} - 3d$ (t_{2g} and e_g orbitals) transitions, respectively. Cathode material LiMn_2O_4 is known for showing 50–50% of Mn^{+3} and Mn^{+4} valence states [12]. In L_3 absorption edge, We have observed two peaks at 642.30 eV and 643.39 eV in LiMn_2O_4 which are identical to peaks at 642.37 in Mn_2O_3 and 643.45 eV in MnO_2 [31]. It shows the presence of Mn^{+3} and Mn^{+4} valence states in $\text{Li}_2\text{Mn}_2\text{O}_4$ [31]. In Li_2MnO_3 ($x=0.0$), we have found peak at 643.45 eV which is comparable to peak observed in MnO_2 , it shows the presence of Mn^{+4} valence state in Li_2MnO_3 . Figure 6b shows the close look of L_3 edge for $\text{Li}_2\text{Mn}_{1-x}\text{Ru}_x\text{O}_3$ [$x=0.0, 0.05, 0.1$]. In $\text{Li}_2\text{Mn}_{0.95}\text{Ru}_{0.05}\text{O}_3$ ($x=0.05$), we have observed peaks at 643.35 eV and in $\text{Li}_2\text{Mn}_{0.9}\text{Ru}_{0.1}\text{O}_3$ ($x=0.1$) we have found peaks at 643.25 eV. These peaks are shifting towards lower energy as Ru concentration is increasing. It confirms the presence of Mn^{+3} valence state along with Mn^{+4} in $\text{Li}_2\text{Mn}_{0.95}\text{Ru}_{0.05}\text{O}_3$ and $\text{Li}_2\text{Mn}_{0.9}\text{Ru}_{0.1}\text{O}_3$.

In Figure 7a, we show Ru- M_4 absorption edge spectra of $\text{Li}_2\text{Mn}_{1-x}\text{Ru}_x\text{O}_3$ [$x=0.05, 0.1$] and $\text{LaMn}_{0.8}\text{Ru}_{0.2}\text{O}_3$ systems together with that of RuO_2 and $\text{Sr}_4\text{Ru}_2\text{O}_9$, where Ru exist in +4 and +5 valence states [11, 15, 32, 33]. The M_4

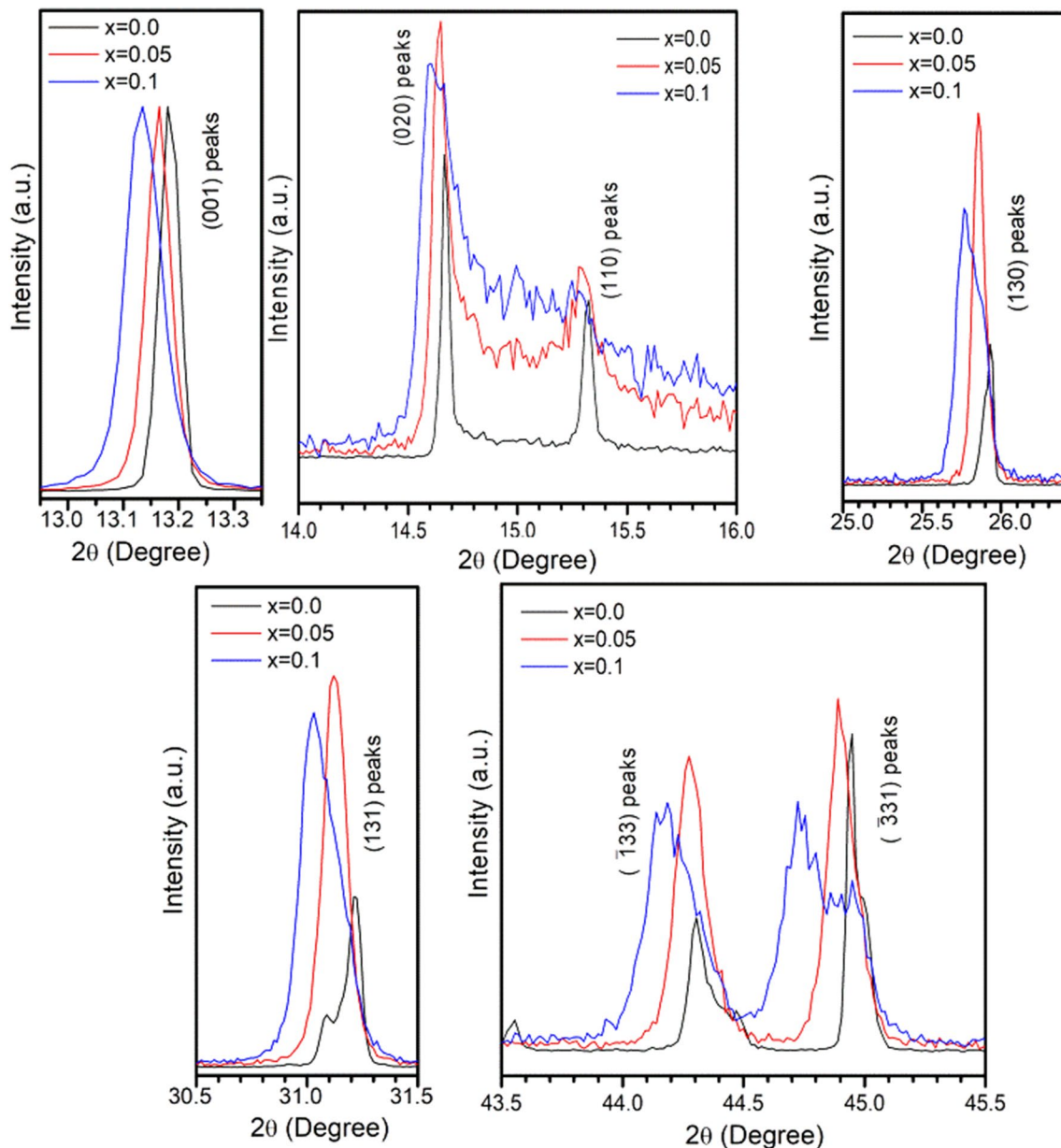


Fig. 3 Zoomed peaks of synchrotron X-ray powder diffraction patterns of $\text{Li}_2\text{Mn}_{1-x}\text{Ru}_x\text{O}_3$ ($x=0.0, 0.05, 0.1$). Shifting of peaks towards lower theta value shows the expansion of lattice with Ru substitution at Mn in Li_2MnO_3

edge and M_5 edge correspond to the electronic transition from Ru- $3d_{5/2}$ to Ru p orbitals and Ru- $3d_{3/2}$ to Ru p orbitals respectively. The M_4 edge of RuO_2 has been found at 287.95 eV which is similar with the reported by Zhou et al. [33]. Zhou et al. have found M_4 edge of Ru at 288 eV in RuO_2 nano particles [33]. The M_4 absorption edge has been found at 289.74 eV for $\text{Sr}_4\text{Ru}_2\text{O}_9$, which is 1.78 eV more than M_4 edge peak of RuO_2 . This result shows the presence of +5 valence state of Ru in $\text{Sr}_4\text{Ru}_2\text{O}_9$. These results are similar

with findings of Hu et al. [32] where they have shown that Ru remains in +4 and +5 valence states for RuO_2 and $\text{Sr}_4\text{Ru}_2\text{O}_9$ respectively [32, 34]. In our observation, $\text{LaMn}_{0.8}\text{Ru}_{0.2}\text{O}_3$ has been found showing M_4 absorption peak of Ru at 288.05 eV which is very close to the absorption peak (at 287.95 eV) of RuO_2 [33]. This result is very much similar with the reported result by Patra et al., where it has been found that Ru remains in +4 valence state in $\text{LaMn}_{0.8}\text{Ru}_{0.2}\text{O}_3$ [21]. In $\text{Li}_2\text{Mn}_{0.95}\text{Ru}_{0.05}\text{O}_3$ ($x=0.05$), we have

Table 1 Synchrotron X-ray powder diffraction data acquisition conditions and lattice parameters of $\text{Li}_2\text{Mn}_{1-x}\text{Ru}_x\text{O}_3$

	Li_2MnO_3	$\text{Li}_2\text{Mn}_{0.95}\text{Ru}_{0.05}\text{O}_3$	$\text{Li}_2\text{Mn}_{0.9}\text{Ru}_{0.1}\text{O}_3$
Space group	C2/m	C2/m	C2/m
a (Å)	4.938	4.944	4.946
b (Å)	8.542	8.561	8.592
c (Å)	5.032	5.037	5.048
β (deg)	109.34	109.30	109.43
Angle range	10 to 70	10 to 70	10 to 70
Step size (deg)	0.015	0.015	0.015
X-ray wavelength (Å)	1.09 Å	1.09 Å	1.09 Å
Crystallite size (nm)	135.29	107.34	74.25

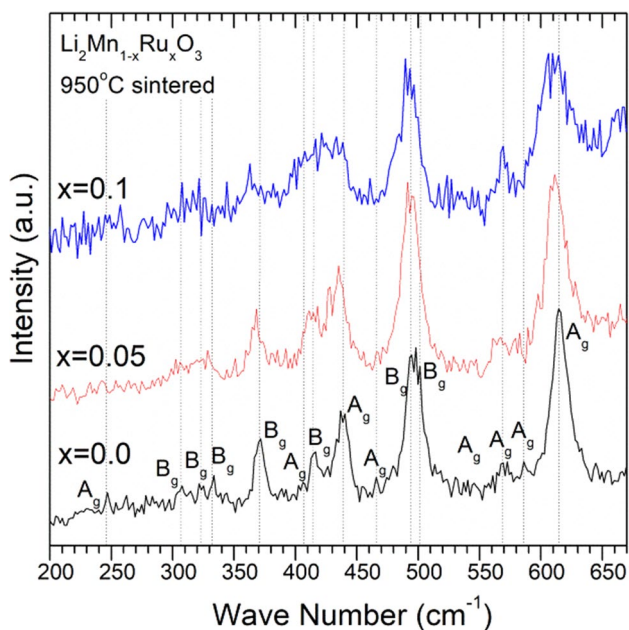


Fig. 4 Raman shift for powder samples of $\text{Li}_2\text{Mn}_{1-x}\text{Ru}_x\text{O}_3$ ($x=0.0, 0.05, 0.1$). Vertical lines show the peak positions for Li_2MnO_3

Table 2 Frequencies of experimentally observed Raman active modes of $\text{Li}_2\text{Mn}_{1-x}\text{Ru}_x\text{O}_3$

Symmetry	Frequency (cm^{-1}) theory [28, 29]	Frequency (cm^{-1}) experiment		
		x=0.0	x=0.05	x=0.1
A_g	621.41	614.7	610.8	609.3, 597.7
	577.03	569.06	565.2	568.05
	448.43	439.25	435.4, 426.9	433.1, 421.2
B_{2g}	498.39	501.8	495.7	494.19
	496.74	494.2	491.4	484.5
	425.98	413.6	412.7	Multiple peaks
	376.98	370.9	368.2	362.5

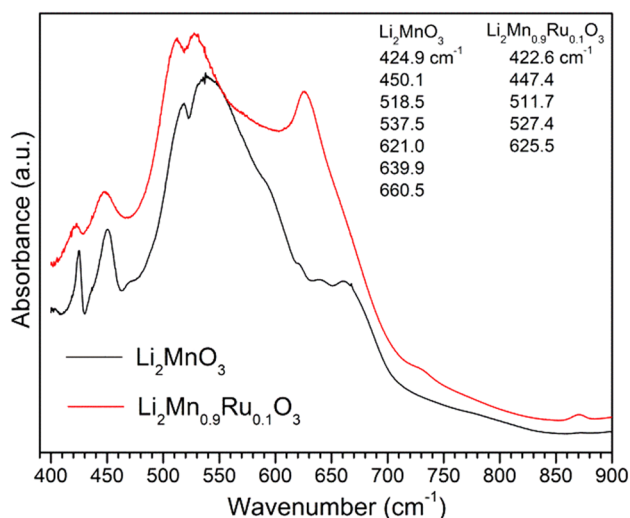


Fig. 5 Peaks of Infrared spectra for powder samples of $\text{Li}_2\text{Mn}_{1-x}\text{Ru}_x\text{O}_3$ ($x=0.0, 0.1$)

observed multiple peaks at 288.15 and 289.88 eV and similarly in ($x=0.1$) two peaks at 288.02 and 289.88 eV have been observed. These two absorption peaks are similar with the M_4 absorption peak of RuO_2 and $\text{Sr}_4\text{Ru}_2\text{O}_9$. These results show that $\text{Li}_2\text{Mn}_{0.9}\text{Ru}_{0.1}\text{O}_3$ and $\text{Li}_2\text{Mn}_{0.95}\text{Ru}_{0.05}\text{O}_3$ contain multi valence states of Ru (Ru^{+4} and Ru^{+5}). Fitting of M_4 absorption peak of Ru shows the % amount of Ru valence state in $\text{Li}_2\text{Mn}_{0.9}\text{Ru}_{0.1}\text{O}_3$ and $\text{Li}_2\text{Mn}_{0.95}\text{Ru}_{0.05}\text{O}_3$ (Fig. 7b). $\text{Li}_2\text{Mn}_{0.95}\text{Ru}_{0.05}\text{O}_3$ compound contains 48% Ru^{+4} valence state and 52% Ru^{+5} valence state. $\text{Li}_2\text{Mn}_{0.9}\text{Ru}_{0.1}\text{O}_3$ compound contains 32% Ru^{+4} valence state and 68% Ru^{+5} valence state.

To see the effect of multivalence states of Ru and Mn in $\text{Li}_2\text{Mn}_{1-x}\text{Ru}_x\text{O}_3$ [$x=0.05, 0.1$] on the transport properties of Li_2MnO_3 , we have measured the frequency dependent impedance measurements. Figure 8 shows the impedance and capacitance for these compositions in the frequency range 10^3 to $4 \times 10^7 \text{ cm}^{-1}$. At frequency 10^3 Hertz, $x=0.0$ composition show $1.38 \times 10^7 \text{ Ohm}$ impedance while $x=0.05$ and 0.1 show 2.82×10^5 and $5.37 \times 10^4 \text{ Ohm}$ respectively. Capacitance is found $1.05 \times 10^{-11} \text{ F}$ at frequency 10^3 Hertz for $x=0.0$ composition while $x=0.05$ and 0.1 compositions show $5.15 \times 10^{-10} \text{ F}$ and $2.71 \times 10^{-9} \text{ F}$ respectively. These measurements show the decrease in impedance and increase in capacitance with the substitution of Ru in Li_2MnO_3 . On increasing frequency, impedance further decreases for all the compositions. These observations confirm the presence of Mn^{+3} valence state along with Mn^{+4} valence state in Ru doped compositions. While synthesis of $\text{Li}_2\text{Mn}_{1-x}\text{Ru}_x\text{O}_3$ [$x=0.0, 0.05, 0.1$] compositions, we have observed that parent $x=0.0$ composition is in reddish colour and Ru doped compositions $x=0.05$ and 0.1 are in black colour. To find out the absorption capability in

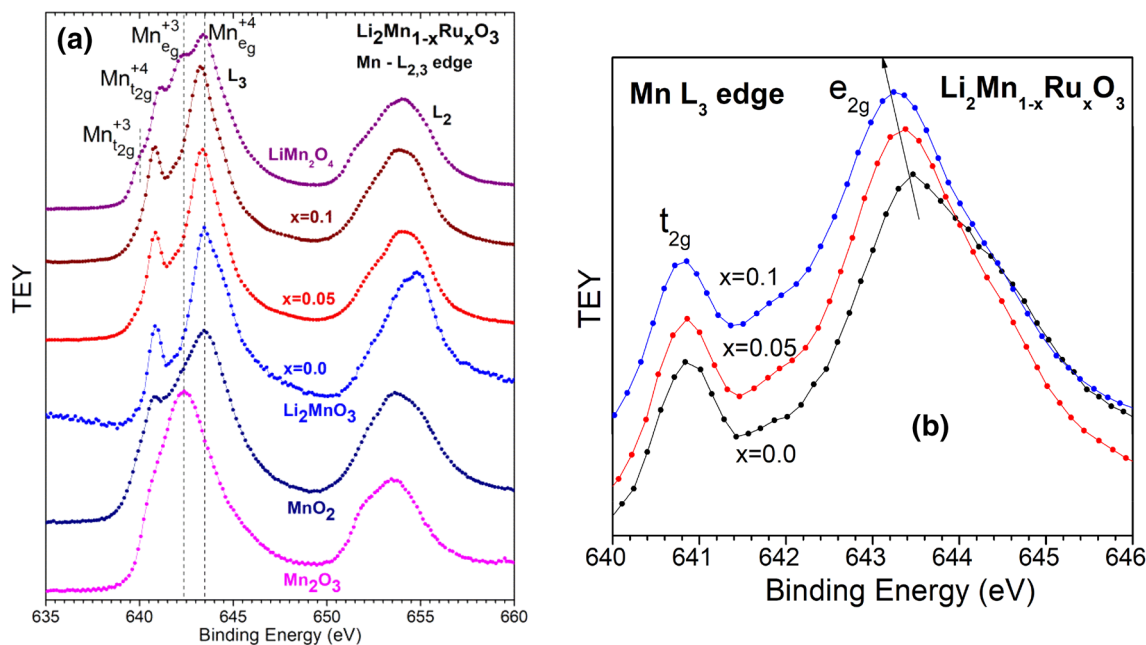


Fig. 6 **a** XAS spectra of $L_{2,3}$ edge for $Li_2Mn_{1-x}Ru_xO_3$ [$x=0.0, 0.05, 0.1$] and $LiMn_2O_4$. XAS spectra of MnO_2 and Mn_2O_3 used for reference of Mn^{+3} and Mn^{+4} valence states peaks. **b** L_3 edge of Ru doped Li_2MnO_3 compositions, which show shift in Mn peaks with Ru substitution

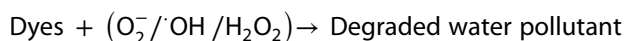
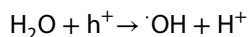
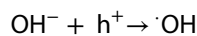
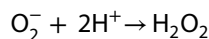
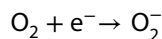
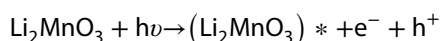
visible light, we have measured UV–vis diffuse reflectance spectroscopic measurements.

Figure 9 shows the reflectance of the $Li_2Mn_{1-x}Ru_xO_3$ [$x=0.0, 0.05, 0.1$] compositions. TiO_2 (commercial sample) is used as reference for reflectance. Optical reflectance spectra of Li_2MnO_3 showed a sharp edge at 610 to 750 nm, which is similar with the reported by Tamilarasan et al. [35]. The peaks ~610 nm corresponds to a HOMO–LUMO gap between filled $O(2p)$ states and empty $Mn(IV)$ ($3d-4s$) states. Figure 10 shows the band gap of the $Li_2Mn_{1-x}Ru_xO_3$ [$x=0.0, 0.05, 0.1$] compositions, which was calculated using Kubelka–Munk function and Tauc plot [22, 23]. Tauc plot gave an energy band gap 2.17 eV for parent Li_2MnO_3 which is in agreement with the theoretical estimations [35, 36]. In Ru doped compositions, we have observed some more reflectance peaks near to 480 nm and 577 nm. Band gap calculation suggests the presence of multiple absorption of band gap 1.97, 2.15, 2.33 and 2.41 eV for $x=0.1$ composition and band gap 1.91, 2.09 and 2.24 eV for $x=0.05$ composition. These experimental determined optical band gaps are reported by theoretical studies on the systems which have Mn mixed valences.

The optical absorption in Mn containing systems is controlled by electric dipole matrix elements that preserve spins of electrons. Features observed in optical conductivity close to 1 eV, 3 eV have been ascribed due to the d–d charge transfer between Mn ions on different sites, e_g-e_g

transitions in perovskite manganite systems [37–39]. These band gap values 1.91, 2.09 and 2.24 eV for $x=0.05$ composition and band gap 1.97, 2.15, 2.33 and 2.41 eV for $x=0.1$ composition suggest the optical activity of $Li_2Mn_{1-x}Ru_xO_3$ [$x=0.05, 0.1$] compositions in visible light.

Ranjeh et al. have investigated photocatalytic properties of Li_2MnO_3 bulk and nano particles using aqueous solution via visible light for degradation of dyes acid red88 and malachite green [40]. Acid red dye degradation was found 17.6% by bulk Li_2MnO_3 and 40.9% by nano Li_2MnO_3 . They have shown following mechanism of degradation using Li_2MnO_3 : [40]



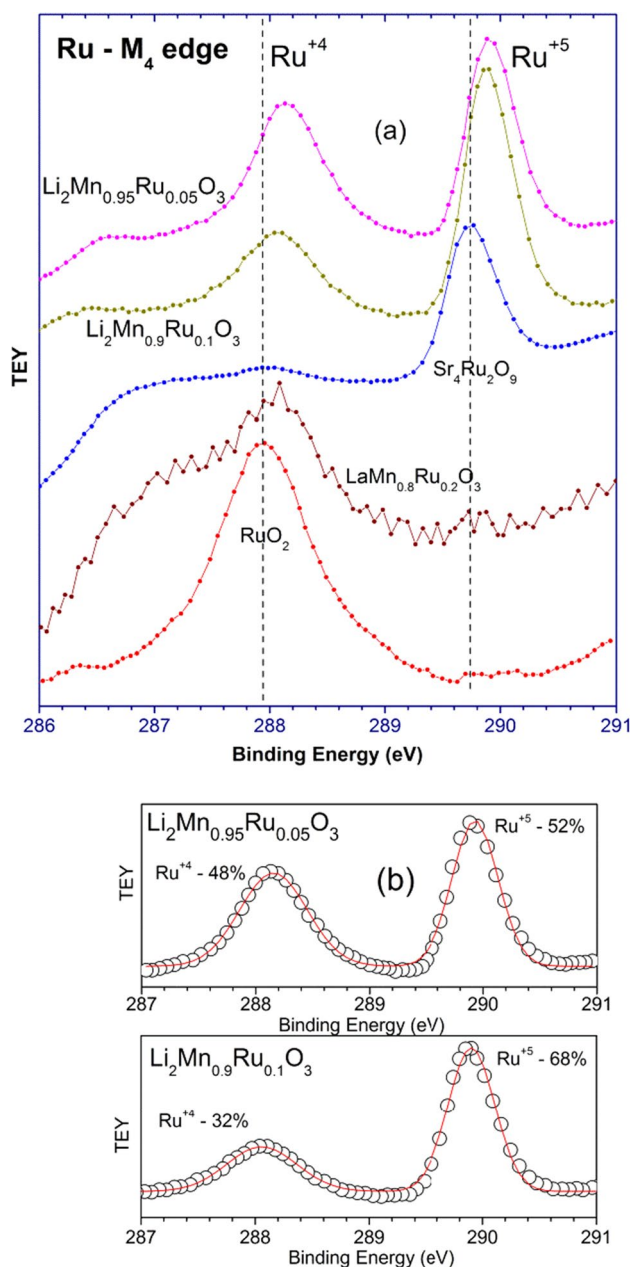


Fig. 7 **a** XAS spectra of M_4 edge for $\text{Li}_2\text{Mn}_{1-x}\text{Ru}_x\text{O}_3$ [$x=0.05, 0.1$]. XAS spectra of RuO_2 and $\text{Sr}_4\text{Ru}_2\text{O}_9$ used for reference of Ru^{+4} and Ru^{+5} valence states peaks. **b** Fitting of Ru —XAS spectra shows the percentage of Ru^{+4} and Ru^{+5} valence states. Circles show the experimental data and red line shows the final peak sum of fit on experimental data

It has been shown that cationic additive enhances the degradation capability of Li_2MnO_3 . These cations make positive surface of Li_2MnO_3 and prevent electron–hole recombination which help generation of OH on the Li_2MnO_3 surface [40]. We have selected two different type

of dyes, (i) A cationic dye, Methylene Blue (MB) and (ii) an azo dye methyl orange (MO) for degradation capabilities of Li_2MnO_3 and its Ru doped compositions. MB is used for printing, leather and in dyeing cotton and, causes various harmful effects such as eye burns, irritation to the skin and gastrointestinal tract [41]. MB is also regarded as significant threat due to its carcinogenic and mutagenic properties [42]. MB containing waste water from industry is essentially needed an efficient treatment technology which give ultimately clean water for safe disposal quickly. Methyl orange is used as an indicator for acid base titration.

In Figure 11, we have plotted the absorption in the wavelength range 200–800 nm of (i) as prepared MO solution (ii) pH controlled (pH=6) MO solution and (iii) MO solution of pH6 mixed with $\text{Li}_2\text{Mn}_{0.9}\text{Ru}_{0.1}\text{O}_3$ composition exposed up to 5 min in visible light. Methyl orange absorbs UV–vis light at ~ 270 nm and ~ 465 nm which corresponds to $n\text{-}\pi^*$ transition. MO solution shows absorption peak ~ 465 nm which shifts to ~ 507 nm after adjusting the pH 6 of the MO solution. After 5 min of ultrasonication and exposure in visible light, MO solution with pH 6 is degraded and no peaks at ~ 465 and ~ 507 nm is visible. $\text{Li}_2\text{Mn}_{0.9}\text{Ru}_{0.1}\text{O}_3$ composition degrades MO solution 100% in 5 min in the presence of nominal pH6. As prepared MO solution show no degradation either in sunlight or with ultrasonication (Table 3).

In Figure 12, we have plotted the absorption of the MB solution mixed with $\text{Li}_2\text{Mn}_{0.9}\text{Ru}_{0.1}\text{O}_3$ composition varied time (b) 1 min (c) 2 min (d) 3 min exposure in visible light. Methylene blue show absorption band at high energy due to $\pi\text{-}\pi^*$ transition of benzene ring while low energy band $\sim 660\text{--}670$ nm corresponds to $n\text{-}\pi^*$ transitions (where n is the free doublet on the nitrogen atom of $\text{C}=\text{N}$ bond and free doublet of S atom on $\text{S}=\text{C}$ bond). Insets show the zoomed plot in the wavelength range 400 to 800 nm for corresponding time exposure in visible light. After 1 min of exposure in visible light, MB peak ($\lambda = 663$ nm) shifts to 619 nm and absorption is very much decreased. After 3 min exposure of visible light, MB is degraded. As prepared MB solution shows no degradation with ultrasonication (Table 4). We have also recorded the degradation using MB solutions (pH6) exposed in Tungston bulb light for 60 min each with (b) Li_2MnO_3 , where Mn is present in +4 valence state (c) LiMn_2O_4 , where Mn is present in +3 and +4 valence states and (d) MnO_2 , where Mn is present in +4 valence state. We have found that there is no substantial degradation of MB solution with Li_2MnO_3 and LiMn_2O_4 while MnO_2 degrades partially in 60 min.

In Figure 13, we show the efficiency for MB in presence of (i) $\text{Li}_2\text{Mn}_{0.9}\text{Ru}_{0.1}\text{O}_3$, where Mn is present in mixed valence

Fig. 8 **a** Impedance **b** capacitance versus frequency plots for $\text{Li}_2\text{Mn}_{1-x}\text{Ru}_x\text{O}_3$ [$x=0.0, 0.05, 0.1$] compositions

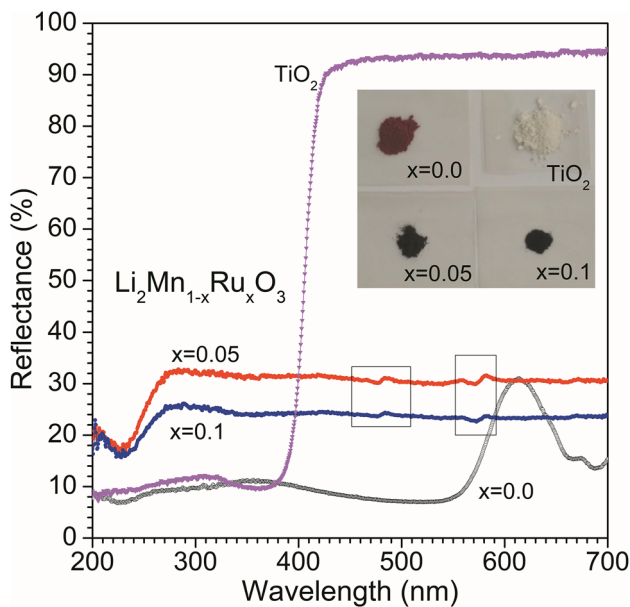
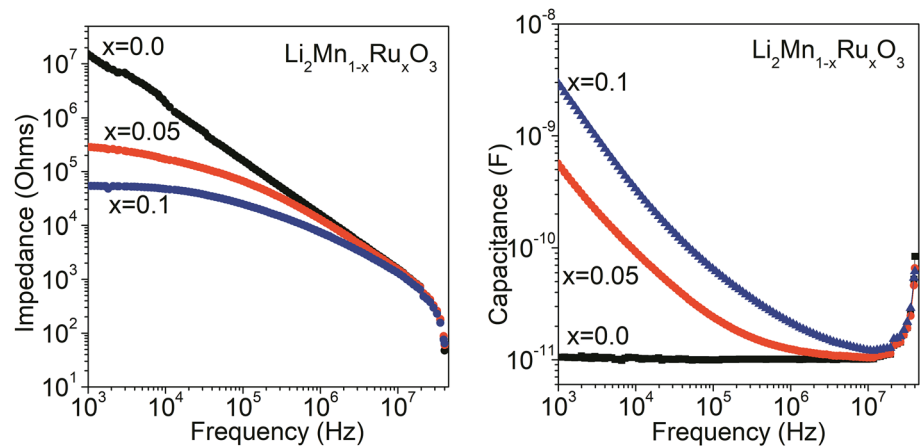


Fig. 9 UV-vis (DRS) spectra for $\text{Li}_2\text{Mn}_{1-x}\text{Ru}_x\text{O}_3$ [$x=0.0, 0.05, 0.1$] compositions. TiO_2 used as a reference

state +3 and +4, and Ru is in mixed valence state +4/+5 (ii) Li_2MnO_3 , where Mn is present in +4 valence state and (iii) LiMn_2O_4 where Mn is present in +3 and +4 valence states. $\text{Li}_2\text{Mn}_{0.9}\text{Ru}_{0.1}\text{O}_3$ (Mixed valences containing oxide) shows very fast decomposition of Methylene blue at nominal pH 6, which was not observed with this efficiency earlier in this type of crystalline materials [40].

Synchrotron X-ray diffraction analysis and Raman spectroscopy measurements show the change in structure with the doping of Ru at Mn site in $\text{Li}_2\text{Mn}_{1-x}\text{Ru}_x\text{O}_3$ [$x=0.05, 0.1$]. XRD studies show the change in lattice which suggest the presence of Ru with Mn in the lattice of $\text{Li}_2\text{Mn}_{1-x}\text{Ru}_x\text{O}_3$ [$x=0.05, 0.1$] systems. XAS studies

show the presence of $\text{Ru}^{+4}/\text{Ru}^{+5}$ and $\text{Mn}^{+3}/\text{Mn}^{+4}$ redox couples in Ru doped materials. When Ru^{+4} doped at Mn^{+4} site, due to comparable redox potential of $\text{Ru}^{+4}/\text{Ru}^{+5}$ (1.07 eV) with that of $\text{Mn}^{+3}/\text{Mn}^{+4}$ (1.02 eV), Ru^{+4} (0.62 Å) converts into Ru^{+5} (0.565 Å) and for charge valence same amount of Mn^{+4} (0.53 Å) converts into Mn^{+3} (0.645 Å) [11, 15]. When Ru^{+4} doped at Mn^{+3} site in LaMnO_3 then mixed valence is not observed as shown in Fig. 7 and it also show by patra et al. [21]. It has been shown earlier that Mn^{+3} (0.645 Å) (in octahedral coordinated configuration) has comparatively bigger radius than Mn^{+4} (0.53 Å) and it has an electron in e_g orbital. Due to one e_g electron, $\text{Mn}^{+3}-\text{O}_6$ octahedral elongate in z axis direction and it brings distortion in lattice. Although, the presence of Ru^{+5} (0.565 Å) make up charge balance but due to size mismatch with Mn^{+3} (0.645 Å) could not stop distortion in lattice of $\text{Li}_2\text{Mn}_{1-x}\text{Ru}_x\text{O}_3$ [$x=0.05, 0.1$]. Raman and IR spectroscopic studies show the evidence of lattice distortion by changing the peak position and splitting in Ru doped compositions.

Impedance has been observed 10^2 times less in $\text{Li}_2\text{Mn}_{0.9}\text{Ru}_{0.1}\text{O}_3$ in comparison to that of Li_2MnO_3 due to the bigger d orbitals of Ru in comparison to Mn and mixed valences $\text{Ru}^{+4}/\text{Ru}^{+5}$ and $\text{Mn}^{+3}/\text{Mn}^{+4}$. Electrons can easily hop in Ru assisted environment in $\text{Li}_2\text{Mn}_{1-x}\text{Ru}_x\text{O}_3$ in comparison to Li_2MnO_3 . Mn^{+3} contains 3 electrons in t_{2g} orbitals while 1 electron in e_g orbitals while Mn^{+4} contains only 3 electrons in t_{2g} orbitals. Ru^{+4} contains 2 paired and 2 unpaired electrons in t_{2g} orbitals while Ru^{+5} contains only 3 electrons in t_{2g} orbitals. One e_g electron of Mn^{+3} can hop to vacant e_g orbitals Mn^{+4} and Ru^{+5} in Ru doped Li_2MnO_3 compositions. One e_g electron of Mn^{+3} and presence of 4d orbitals containing Ru modify the impedance and capacitance properties of Ru doped Li_2MnO_3 compositions.

Fig. 10 Band gap calculations using UV-vis (DRS) spectra for **a** $F(R)$ for all the compositions **b** $x=0.0$, **c** $x=0.05$ **d** $x=0.1$ in $\text{Li}_2\text{Mn}_{1-x}\text{Ru}_x\text{O}_3$ [$x=0.0, 0.05, 0.1$] compositions

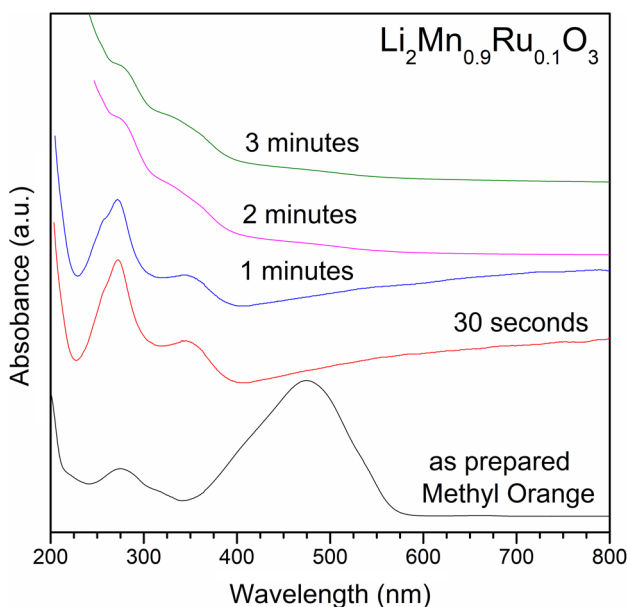
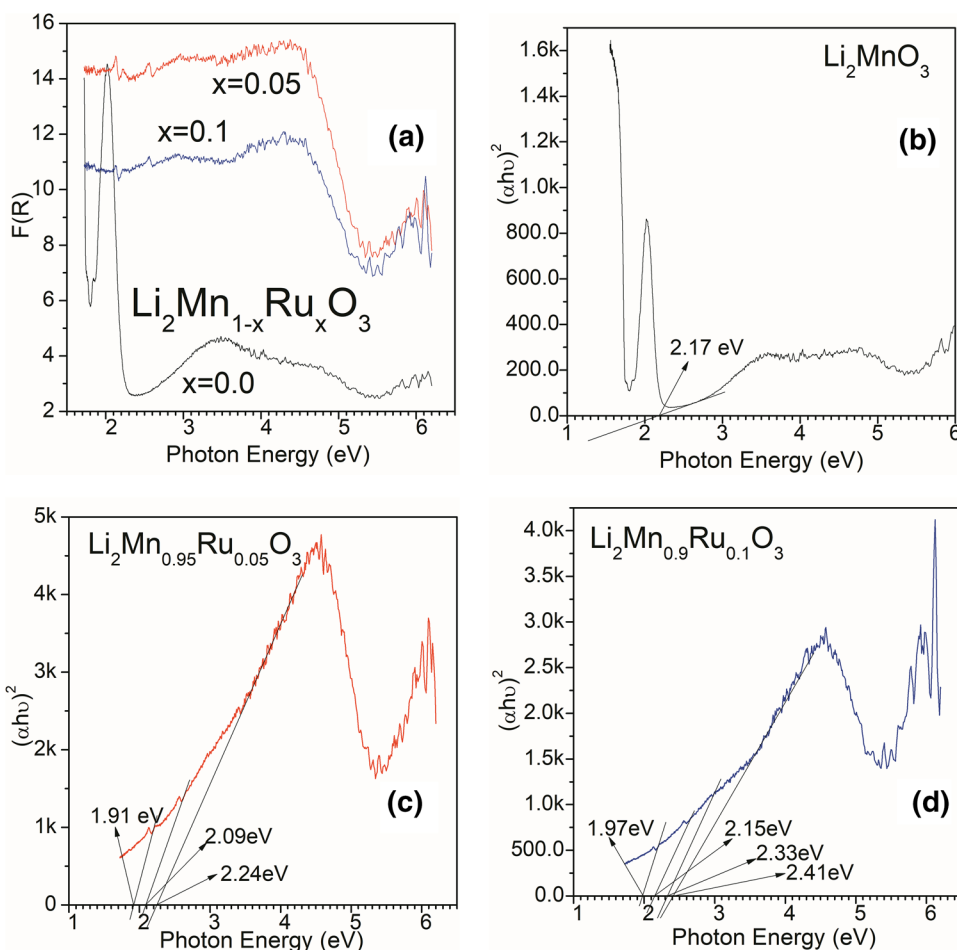


Fig. 11 Absorbance spectra of the Methyl Orange solutions after reaction with $\text{Li}_2\text{Mn}_{0.9}\text{Ru}_{0.1}\text{O}_3$ in the given exposure time of W bulb light. Please note disappearance of peak ~ 450 nm on 30 s of exposure of W bulb light

Diffuse reflectance spectroscopic studies suggest the optical absorption in visible light in $\text{Li}_2\text{Mn}_{1-x}\text{Ru}_x\text{O}_3$ [$x=0.0, 0.05, 0.1$] systems. Band gap increases with the increase of Ru content while crystallite size decreased. In the crystalline environment of Ru and Mn in $\text{Li}_2\text{Mn}_{1-x}\text{Ru}_x\text{O}_3$ [$x=0.05, 0.1$], Mn intersite and Ru intersite transitions using $e_g - e_g, t_{2g} - e_g$ may become allowed by spin orbit coupling, lattice disorder/distortions and mixing of odd parity wave functions. Decreases in crystallite size of the compositions, Mn–Mn intersite, Ru–Mn intersite and spin orbit coupling are the main cause of enhanced band gap of $\text{Li}_2\text{Mn}_{0.9}\text{Ru}_{0.1}\text{O}_3$ and $\text{Li}_2\text{Mn}_{0.95}\text{Ru}_{0.05}\text{O}_3$ in comparison to Li_2MnO_3 .

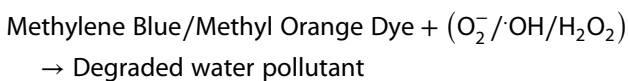
Presence of mixed valences $\text{Ru}^{+4}/\text{Ru}^{+5}$ and $\text{Mn}^{+3}/\text{Mn}^{+4}$ assist the process of degradation of MO and MB solutions with faster rate in comparison with MnO_2 . Compounds $\text{LaMn}_{1-x}\text{Ru}_x\text{O}_3$ degrades MO dye only at pH 2.5 and takes 15 min [21]. $\text{LaMn}_{1-x}\text{Ru}_x\text{O}_3$ shows the presence of only Mn^{+3} and Ru^{+4} valence states. Our results show the presence of redox couples $\text{Mn}^{+3}-\text{Mn}^{+4}$ and $\text{Ru}^{+4}-\text{Ru}^{+5}$ valence states in $\text{Li}_2\text{Mn}_{1-x}\text{Ru}_x\text{O}_3$ [$x=0.05, 0.1$]. Multiple valence states enhance the process of degradation of 5 ml each of MO and MB dyes in $\text{Li}_2\text{Mn}_{1-x}\text{Ru}_x\text{O}_3$ [$x=0.05, 0.1$]. 5 mg of

Table 3 Degradation profile of Methyl Orange (MO) dye with $\text{Li}_2\text{Mn}_{1-x}\text{Ru}_x\text{O}_3$ and MnO_2 in different experimental conditions

Conditions for methyl orange (MO) degradation	Degradation time with compounds		
	$\text{Li}_2\text{Mn}_{0.9}\text{Ru}_{0.1}\text{O}_3$	Li_2MnO_3	MnO_2
In the presence of sunlight (solution pH-6)	~5 min	~30 min	~30 min
In the presence of sunlight (as prepared solution)	No degradation in 1 h	No degradation in 1 h	No degradation in 1 h
Ultrasonicated in W bulb light (solution pH-6)	~3 min	~60 min	No degradation in 1 h
Without ultrasonication exposed in W bulb (solution pH-6)	~5 min	~60 min	
Ultrasonicated in W bulb (as prepared solution)	No Degradation in 1 h	No degradation in 1 h	
Ultrasonicated in dark (absence of light) solution pH-6	30 min	~60 min	

$\text{Li}_2\text{Mn}_{0.9}\text{Ru}_{0.1}\text{O}_3$ degrades 5 ml of MO (10 mg/L) up to 100% in 5 min and 5 ml of MB (10 mg/L) in 3 min at pH 6. 5 mg of MnO_2 does not degrade 5 ml of MO (10 mg/L) in 60 min and 5 ml of MB (10 mg/L) in 60 min at pH 6 [Tables 3, 4; Fig. 13]. 20 mg of flower like Mn_3O_4 (where Mn in Mn^{+3} valence state) degrades 50 ml MB (10 mg/L) up to 80% in 180 min in presence of H_2O_2 [8]. 100 mg nano wires of MnO_2 (where Mn in Mn^{+4} valence state) degrades 200 ml MO (40 mg/L) up to 100% in 90 min [9].

Possible degradation mechanism can be summarised by following reactions as shown by Ranjeh et al.:



Presence of multiple valence states $\text{Mn}^{+3}/\text{Mn}^{+4}$ and $\text{Ru}^{+4}/\text{Ru}^{+5}$ create photo generated electrons and holes by transferring electrons from valence band to conduction band leaving holes in valence band. Electrons react with O_2 and generate O_2^- . O_2^- further reacts with H^+ ions and generates H_2O_2 . Holes react with OH^- and generate OH^\cdot free radicals. So $(\text{O}_2^-/\cdot\text{OH}/\text{H}_2\text{O}_2)$ react with MO, MB dyes solution and decolourize. If H^+ ions are not present then these compounds does not degrade MO and MB dyes. In presence of H^+ and visible light, Li_2MnO_3 does not degrade MO and MB dyes up to 24 h. $\text{Li}_2\text{Mn}_{1-x}\text{Ru}_x\text{O}_3$ [$x=0.05, 0.1$] degrades MO and MB dyes very fast in presence of H^+ (pH 6) and W bulb/sunlight due to presence of mixed

valence states $\text{Mn}^{+3}/\text{Mn}^{+4}$ and $\text{Ru}^{+4}/\text{Ru}^{+5}$. These materials degrades MB dye very fast in compare to other Mn based systems Mn_3O_4 , MnO_2 and nano Li_2MnO_3 [8, 9, 43]. Easy material preparation of $\text{Li}_2\text{Mn}_{1-x}\text{Ru}_x\text{O}_3$ and reusability of these materials is an advantage over other known TiO_2 based catalysts.

4 Conclusions

We have optimized the synthesis conditions for inducing the redox interaction between Ru^{+4} and Mn^{+4} which further results $\text{Mn}^{+3}-\text{Mn}^{+4}$ and $\text{Ru}^{+4}-\text{Ru}^{+5}$ valence states in $\text{Li}_2\text{Mn}_{1-x}\text{Ru}_x\text{O}_3$ [$x=0.05, 0.1$]. These redox couples in presence of H^+ ions and W bulb/sunlight enhances the dye degradation process in Ru doped Li_2MnO_3 . $\text{Li}_2\text{Mn}_{0.9}\text{Ru}_{0.1}\text{O}_3$ composition (i) shows 10^2 times decreased impedance and (ii) quickly degrades methyl orange and methylene blue solutions at pH 6 which shows its capability as effective dye degradation material which otherwise was neither found in other Mn based systems nor in these types of monoclinic crystals. These Ru doped $\text{Li}_2\text{Mn}_{1-x}\text{Ru}_x\text{O}_3$ materials can be use for fast decomposition of other organic dyes which are harmful for environment. Fast degradation of dyes, easy material preparation and reusability can make these materials first choice in industry over other known TiO_2 based catalysts.

Fig. 12 Absorption spectra of the MB solutions during the decomposition reaction catalyzed by $\text{Li}_2\text{Mn}_{0.9}\text{Ru}_{0.1}\text{O}_3$ in the exposure of visible light for (b) 1 (c) 2 and (d) 3 min

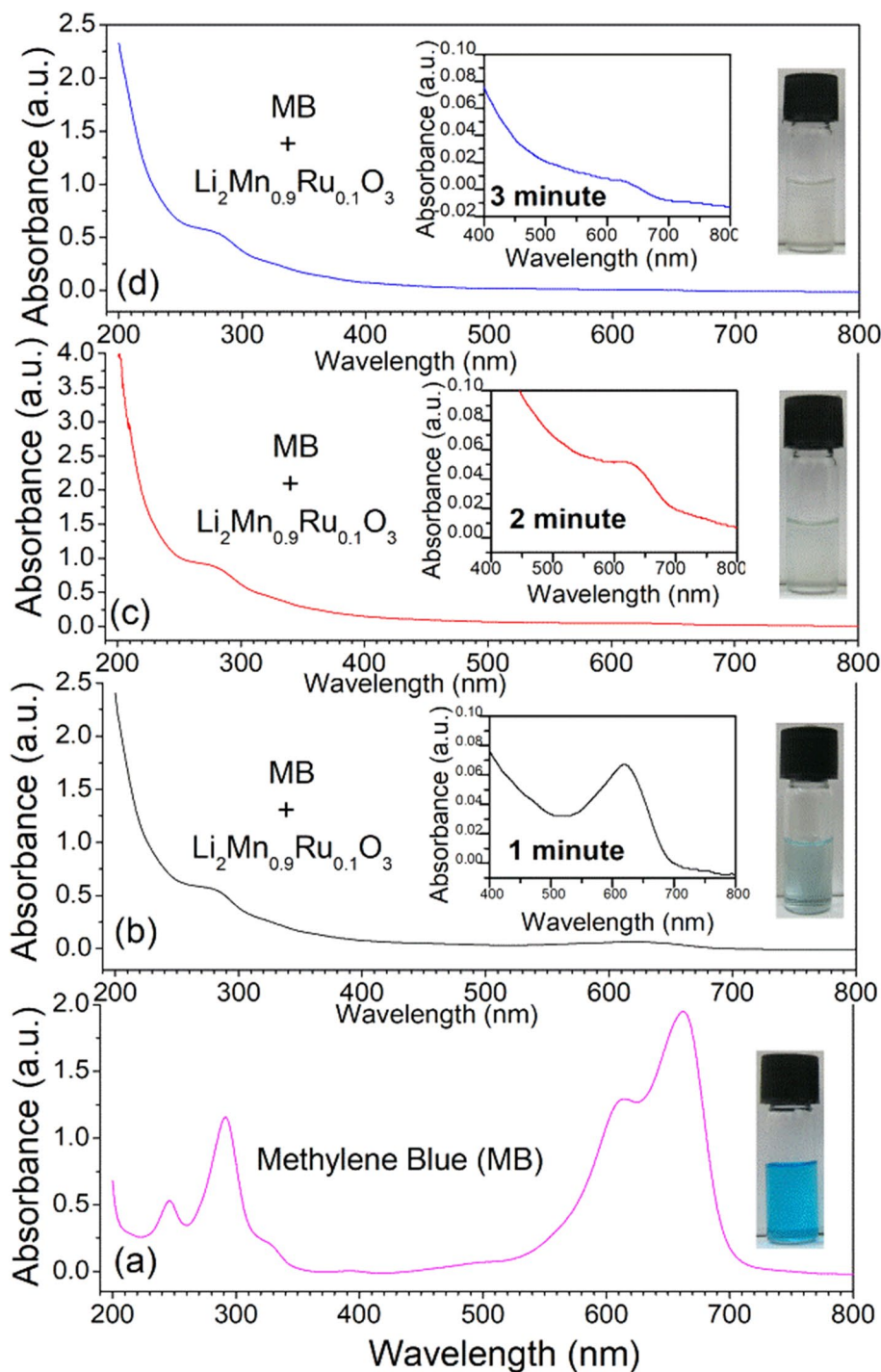
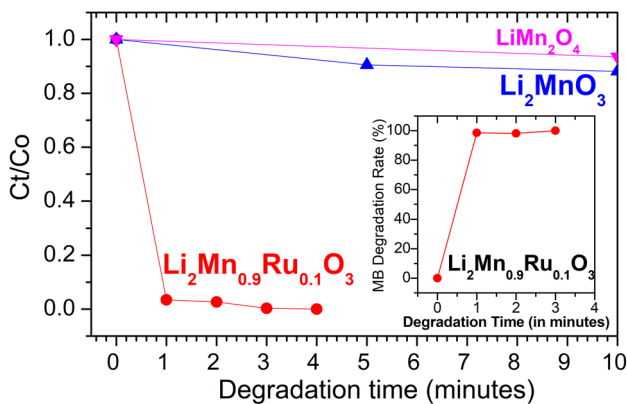


Table 4 Degradation profile of methylene blue (MB) dye with $\text{Li}_2\text{Mn}_{1-x}\text{Ru}_x\text{O}_3$ and MnO_2 in different experimental conditions

Conditions for Methylene Blue (MB) degradation	Degradation time with compounds		
	$\text{Li}_2\text{Mn}_{0.9}\text{Ru}_{0.1}\text{O}_3$	Li_2MnO_3	MnO_2
In the presence of sunlight (solution pH-6)	~60 min	No degradation in 1 h	No degradation in 1 h
In the presence of sunlight (as prepared solution)	Partial degradation in 1 h	No degradation in 1 h	
Ultrasonicated in W bulb light (solution pH-6)	~3 min	No degradation in 2 h	2 h
Without ultrasonication exposed in W bulb light (solution pH-6)	~60 min		No complete degradation in 2 h
Ultrasonicated in W bulb light (as prepared solution)	No degradation in 2 h		
Ultrasonicated in dark (absence of light) solution pH-6	~30 min		

**Fig. 13** Degradation rate of MB solutions [5 ml of 10 mg/L concentration] under visible light irradiation with 5 mg $\text{Li}_2\text{Mn}_{0.9}\text{Ru}_{0.1}\text{O}_3$, Li_2MnO_3 and LiMn_2O_4 each

Acknowledgements P. Singh thanks to the UGC-DAE-Consortium for Scientific Research (CSR), Indore Centre for project fellowship and B. Singh thanks for providing financial support under the CRS project scheme. B. Singh thanks Department of Science and Technology, India for the financial support and Saha Institute of Nuclear Physics, India for facilitating the experiments at the Indian Beamline, Photon Factory, KEK, Japan. B. Singh thanks to Dr. Mukul Gupta (UGC-DAE-CSR Indore), Dr. D. M. Phase (UGC-DAE-CSR Indore) for help in SXAS experiments and Prof. R. Dhar (Univ. of Allahabad) for UV-visible spectroscopy measurements.

Compliance with ethical standards

Conflict of interest The authors declare "There are no conflicts to declare".

References

- Ellis BL, Lee KT, Nazar LF (2010) Positive electrode materials for Li-ion and Li-batteries. *Chem Mater* 22:691–714
- Coey JMD, Viret M, Molnar VS (1999) Mixed-valence manganites. *Adv Phys* 48:167–293
- Weifeng W, Xinwei C, Weixing C, Douglas GI (2011) Manganese oxide-based materials as electrochemical supercapacitor electrodes. *Chem Soc Rev* 40:1697–1721
- Thackeray MM, David WIF, Bruce PG, Goodenough JB (1983) Lithium insertion into manganese spinels. *Mater Res Bull* 18:461–472
- Jin S, Tiefel TH, McCormack M, Fastnacht RA, Ramesh R, Chen LH (1994) Colossal magnetoresistance in La-Ca-Mn-O ferromagnetic thin films. *Science* 264:413–415
- Millis AJ, Shraiman BI, Mueller R (1996) Dynamic Jahn-Teller effect and colossal magnetoresistance in $\text{La}_{1-x}\text{Sr}_x\text{MnO}_3$. *Phys Rev Lett* 77:175–178
- Tarascon JM, McKinnon WR, Coowar F, Bowmer TN, Amatucci G, Guyomard D (1994) Structural stability of LiMn_2O_4 electrodes for lithium batteries. *J Electrochem Soc* 141:1421–1431
- Wang Y, Zhu L, Yang X, Shao E, Deng X, Liu N, Wu M (2015) Facile synthesis of three-dimensional Mn_3O_4 hierarchical microstructures and their application in the degradation of methylene blue. *J Mater Chem A* 3:2934–2941
- Yin B, Zhang S, Jiao Y, Liu Y, Qu F, Wu X (2014) Facile synthesis of ultralong MnO_2 nanowires as high performance supercapacitor electrodes and photocatalysts with enhanced photocatalytic activities. *Cryst Eng Comm* 16:9999–10005
- Yoo SH, Jang D, Johab HIK, Lee S (2017) Iron oxide/porous carbon as a heterogeneous Fenton catalyst for fast decomposition of hydrogen peroxide and efficient removal of methylene blue. *J Mater Chem A* 5:748–755
- Sahu RK, Hu Z, Rao ML, Manoharan SS, Schmidt T, Richter B, Knupfer M, Golden M, Fink J, Schneider CM (2002) X-ray absorption spectra at the Ru and Mn $L_{2,3}$ edges and long-range ferromagnetism in $\text{SrRu}_{1-x}\text{Mn}_x\text{O}_3$ solid solutions ($0 \leq x \leq 0.5$). *Phys Rev B* 66:144415
- Reddy MV, Manoharan SS, John J, Singh B, Rao GVS, Chowdari BVR (2009) Synthesis, characterization, and electrochemical cycling behavior of the Ru-doped spinel, $\text{Li}[\text{Mn}_{2-x}\text{Ru}_x]\text{O}_4$ ($x = 0, 0.1, \text{ and } 0.25$). *J Electrochem Soc* 156:A652–A660
- Malavasi L, Mozzati MC, Tealdi C, Azzoni CB, Flor G (2005) Influence of Ru doping on the structure, defect chemistry, magnetic interaction, and carrier motion of the $\text{La}_{1-x}\text{Na}_x\text{MnO}_{3+\delta}$ manganite. *J Phys Chem B* 109:20707–20713
- Singh B, Manoharan SS, Rao ML, Pai SP (2004) Long range ferromagnetic ordering in pulsed laser deposited $\text{La}_{0.7}\text{Ca}_{0.3}\text{Mn}_{1-x}\text{Ru}_x\text{O}_3$ thin films. *Phys Chem Chem Phys* 6:4199–4202

15. Manoharan SS, Sahu RK (2002) Evidence for an anomalous redox ionic pair between Ru and Mn in $\text{SrRu}_{0.5}\text{Mn}_{0.5}\text{O}_3$: an X-ray absorption spectroscopy approach. *Chem Commun* 24:3068–3069
16. Mori D, Sakaebeg H, Shikanob M, Kojitania H, Tatsumib K, Inaguma Y (2011) Synthesis, phase relation and electrical and electrochemical properties of ruthenium-substituted Li_2MnO_3 as a novel cathode material. *J Power Sources* 196:6934–6938
17. Sathiya M, Ramesha K, Rouse G, Foix D, Gonbeau D, Prakash AS, Doublet ML, Hemalatha K, Tarascon JM (2013) High performance $\text{Li}_2\text{Ru}_{1-y}\text{Mn}_y\text{O}_3$ ($0.2 \leq y \leq 0.8$) cathode materials for rechargeable lithium-ion batteries: their understanding. *Chem Mater* 25:1121–1131
18. Xu Y, Hu E, Yang F, Corbett J, Sun Z, Lyu Y, Yu X, Liu Y, Yang XQ, Li H (2016) Structural integrity—searching the key factor to suppress the voltage fade of Li-rich layered cathode materials through 3D X-ray imaging and spectroscopy techniques. *Nano Energy* 28:164–171
19. Sathiya M, Rouse G, Ramesha K, Laisa CP, Vezin H, Sougrati MT, Doublet ML, Foix D, Gonbeau D, Walker W, Prakash AS, Hassine MB, Dupont L, Tarascon JM (2013) Reversible anionic redox chemistry in high-capacity layered-oxide electrodes. *Nat Mater* 12:827–835
20. Singh B (2016) Ru^{4+} induced colossal magnetoimpedance in Ru doped perovskite manganite at room temperature. *Phys Chem Chem Phys* 18:12947–12951
21. Patra AS, Gogoi G, Sahu RK, Qureshi M (2017) Modulating the electronic structure of lanthanum manganite by ruthenium doping for enhanced photocatalytic water oxidation. *Phys Chem Chem Phys* 19:12167–12174
22. Kubelka P, Munk F (1931) Ein Beitrag Zur Optik Der Farbanstriche. *Z Techn Phys* 12:593–601
23. Tauc J (1968) Optical properties and electronic structure of amorphous Ge and Si. *Mater Res Bull* 3:37–46
24. Strobel P, Lambert-Andron B (1988) Crystallographic and magnetic structure of Li_2MnO_3 . *J Solid State Chem* 75:90–98
25. Massarotti V, Bini M, Capsoni D, Altomare A, Moliterni AGG (1997) Ab initio structure determination of Li_2MnO_3 from X-ray powder diffraction data. *J Appl Crystallogr* 30:123–127
26. Singh B (2015) Structural, transport, magnetic and magnetoelectric properties of $\text{CaMn}_{1-x}\text{Fe}_x\text{O}_{3-\delta}$ ($0.0 \leq x \leq 0.4$). *RSC Adv* 5:39938–39945
27. Ruther RE, Dixit H, Pezeshki AM, Sacci RL, Cooper VR, Nanda J, Veith GM (2015) Correlating local structure with electrochemical activity in Li_2MnO_3 . *J Phys Chem C* 119:18022–18029
28. Julien CM, Massot M (2003) Lattice vibrations of materials for lithium rechargeable batteries III. Lithium manganese oxides. *Mater Sci Eng, B* 100:69–78
29. Amalraj SF, Sharon D, Talianker M, Julien CM, Burkala L, Lavi R, Zhecheva E, Markovsky B, Zinigrad E, Kovacheva D (2013) Study of the nanosized Li_2MnO_3 : electrochemical behavior, structure, magnetic properties, and vibrational modes. *Electrochim Acta* 97:259–270
30. Saroha R, Gupta A, Panwar AK (2017) Electrochemical performances of Li-rich layered-layered Li_2MnO_3 - LiMnO_2 solid solutions as cathode material for lithium-ion batteries. *J Alloys Compd* 696:580–589
31. Liu RS, Jang LY, Chen JM, Tsai YC, Hwang YD, Liu RG (1997) X-ray absorption studies in spinel-type LiMn_2O_4 . *J Solid State Chem* 128:326–329
32. Hu Z, Lips HV, Golden MS, Fink J, Kaindl G, de Groot FM, Ebbinghaus S, Reller A (2000) Multiplet effects in the Ru $L_{2,3}$ X-ray-absorption spectra of R(IV) and Ru(V) compounds. *Phy Rev B* 61:5262–5266
33. Zhou JG, Fang HT, Hu YF, Sham TK, Wu CX, Liu M, Li F (2009) Immobilization of RuO_2 on carbon nanotube: an X-ray absorption near-edge structure study. *J Phys Chem C* 113:10747–10750
34. Manoharan SS, Singh B, Driscoll J, Branford W, Cohen L, Besmehn A (2005) Magnetism and electronic transport in $\text{Sr}_{4-x}\text{La}_x\text{Ru}_{2-x}\text{Mn}_x\text{O}_9$: interplay of Mn and Ru redox chemistry. *J Appl Phys* 97:10A304
35. Tamilarasan S, Laha S, Natarajan S, Gopalakrishnan J (2015) Li_2MnO_3 : a rare red-coloured manganese (IV) oxide exhibiting tunable red–yellow–green emission. *J Mater Chem C* 3:4794–4800
36. Xiao R, Li H, Chen L (2012) Density functional investigation on Li_2MnO_3 . *Chem Mater* 24:4242–4251
37. Quijada M, Černe J, Simpson JR, Drew HD, Ahn KH, Millis AJ, Shreekala R, Ramesh R, Rajeswari M, Venkatesan T (1988) Optical conductivity of manganites: crossover from Jahn-Teller small polaron to coherent transport in the ferromagnetic state. *Phys Rev B* 58:16093–16102
38. McCormack M, Jin S, Tiefel TH, Fleming RM, Phillips JM, Ramesh R (1994) Very large magnetoresistance in perovskite-like La–Ca–Mn–O thin films. *Appl Phys Lett* 64:3045–3047
39. Prellier W, Mercey B, Lecouer P (2001) Colossal-magnetoresistive manganite thin films. *J Phys: Condens Matter* 13:R915–R944
40. Ranjeh M, Masjedi-Arani M, Salavati-Niasari M, Hossein Moayedi H (2020) EDTA-modified sol-gel synthesis of monoclinic Li_2MnO_3 nanoparticles as an effective photocatalyst for degradation of organic dyes. *J Mol Liq* 300:112292
41. Turhan K, Ozturkcan SA (2013) Decolorization and degradation of reactive dye in aqueous solution by ozonation in a semi-batch bubble column reactor. *Water Air Soil Pollut* 224:1353
42. El Mouzdahir Y, Elmchaouri A, Mahboub R, Gil A, Korili SA (2010) Equilibrium modeling for the adsorption of methylene blue from aqueous solutions on activated clay minerals. *Desalination* 250:335–338
43. Larbi T, Doll K, Amlouk M (2019) Temperature dependence of Raman spectra and first principles study of NiMn_2O_4 magnetic spinel oxide thin films: application in efficient photocatalytic removal of RhB and MB dyes. *Spectrochim Acta Part A Mol Biomol Spectrosc* 216:117–224

Publisher's Note Springer Nature remains neutral with regard to jurisdictional claims in published maps and institutional affiliations.